

**Magnetic phase diagram and crystal-field effects in the kagome-lattice
antiferromagnet $U_3Ru_4Al_{12}$**

Gorbunov, D. I.; Ishii, I.; Nomura, T.; Henriques, M. S.; Andreev, A. V.; Uhlarz, M.;
Suzuki, T.; Zherlitsyn, S.; Wosnitza, J.;

Originally published:

February 2019

Physical Review B 99(2019), 054413

DOI: <https://doi.org/10.1103/PhysRevB.99.054413>

Perma-Link to Publication Repository of HZDR:

<https://www.hzdr.de/publications/Publ-28920>

Release of the secondary publication
on the basis of the German Copyright Law § 38 Section 4.

Magnetic phase diagram and crystal-field effects in the kagome-lattice antiferromagnet $\text{U}_3\text{Ru}_4\text{Al}_{12}$

D. I. Gorbunov,¹ I. Ishii,² T. Nomura,¹ M. S. Henriques,³
A. V. Andreev,³ M. Uhlarz,¹ T. Suzuki,² S. Zherlitsyn,¹ and J. Wosnitza^{1,4}

¹*Hochfeld-Magnetlabor Dresden (HLD-EMFL), Helmholtz-Zentrum Dresden-Rossendorf, 01328 Dresden, Germany*

²*Department of Quantum Matter, ADSM, Hiroshima University, Higashi-Hiroshima 739-8530, Japan*

³*Institute of Physics, Academy of Sciences, Na Slovance 2, 182 21 Prague, Czech Republic*

⁴*Institut für Festkörper- und Materialphysik, TU Dresden, 01062 Dresden, Germany*

We report on the magnetic phase diagram of the distorted kagome-lattice antiferromagnet $\text{U}_3\text{Ru}_4\text{Al}_{12}$ determined through measurements of magnetic and elastic properties. For field applied along the [100] and [120] axes of the hexagonal crystal structure, we find pronounced anomalies in the magnetization and elastic moduli that signal the existence of unknown magnetic phases. Our crystal-electric-field (CEF) analysis evidences interlevel quadrupolar interactions between the ground-state singlet and the first excited doublet. These interactions lead to a large softening of the shear elastic modulus C_{44} . The large number of phases and pronounced elastic softening suggest that geometric frustrations and CEF effects play an important role in the physical properties of $\text{U}_3\text{Ru}_4\text{Al}_{12}$.

I. INTRODUCTION

Geometric frustration refers to the inability of a system to minimize the interaction energy between each pair of spins due to their spatial arrangement. This lowers or even completely suppresses magnetic ordering temperature and may reveal competing interactions and complex ground states. In a geometrically frustrated material, several states with different orders can have similar energies. A small perturbation can therefore significantly affect its electronic properties. An applied magnetic field can act as a tuning parameter between different magnetic phases. Frustrated compounds often exhibit complex phase diagrams and offer a rich playground for studying competing interactions [1–6].

Kagome systems have a corner-sharing triangular lattice. Among intermetallic compounds having a kagome lattice, CePdAl stands out due to the coexistence of geometric frustration and an antiferromagnetic order and its proximity to a quantum critical point [7–9]. Below the Néel temperature, $T_N = 2.7$ K, one third of the partly itinerant Ce magnetic moments are disordered.

Interesting physics can also be expected for uranium-based kagome intermetallic compounds. The $5f$ electron states are usually partially delocalized and participate in bonding. They hybridize with the s , p , and d states of surrounding ligands and conduction electrons. This has as a consequence a dominance of many-body phenomena in the cross-over regime. The $5f$ bandwidth, the screened interatomic Coulomb interaction, the spin-orbit coupling, and the exchange interaction are all on a similar energy scale. Hence, uranium-based intermetallic compounds show a rich variety of ground states and magnetic properties (see, e.g., Ref. [10]).

The ternary intermetallic compound $\text{U}_3\text{Ru}_4\text{Al}_{12}$ crys-

tallizes in a hexagonal crystal structure of $\text{Gd}_3\text{Ru}_4\text{Al}_{12}$ type (space group $P6_3/mmc$; a detailed description of the crystal structure is given in Refs. [11–14]) where the U atoms form a distorted kagome lattice parallel to the basal plane. This crystal structure is well suited to study correlated magnetism in the presence of geometric frustration, as can be inferred from previous studies of isostructural compounds, particularly those with magnetic rare-earth atoms, R . Complex magnetic structures and field-induced magnetic phase transitions accompanied by large anomalies in transport and elastic properties were reported for several members of the $R_3\text{Ru}_4\text{Al}_{12}$ family [16–23]. One might naturally expect $\text{U}_3\text{Ru}_4\text{Al}_{12}$ to show various magnetic phases as applied magnetic field tunes the state of the $5f$ electrons. Although geometric frustration is likely to play a role in the magnetism of $\text{U}_3\text{Ru}_4\text{Al}_{12}$, the compound orders antiferromagnetically below 10 K [14, 15]. The frustration, however, affects the magnetic structure that was found to be noncollinear with the U moments confined to the basal plane.

Here, we use magnetic field as a tuning parameter to explore the phase diagram of $\text{U}_3\text{Ru}_4\text{Al}_{12}$. We employ magnetization and ultrasound measurements in static and pulsed magnetic fields to unveil new phases in the compound. Particularly ultrasound is known to be a highly sensitive probe of magnetoelastic interactions [24–30]. We find pronounced anomalies in the magnetic and elastic properties of $\text{U}_3\text{Ru}_4\text{Al}_{12}$ that allow us to identify three ordered phases in the H - T plane for field applied along the [100] axis and two phases for field applied along the [120] direction. Additionally, our crystal-electric-field (CEF) analysis confirms that quadrupolar interactions are responsible for a pronounced softening of a shear elastic modulus. The large number of phases and the existence of quadrupolar interactions suggest that geometric frustrations and CEF effects play an important role in the physical properties of $\text{U}_3\text{Ru}_4\text{Al}_{12}$.

II. EXPERIMENTAL DETAILS

A $\text{U}_3\text{Ru}_4\text{Al}_{12}$ single crystal was grown from an 8-gram quasi-stoichiometric mixture of the pure elements (99.9% U, 99.99% Ru and 99.999% Al) with an Al mass excess of 1% in a tri-arc furnace by a modified Czochralski method on a rotating water-cooled Cu crucible under protective Ar atmosphere. A tungsten rod was used as a seed. The pulling speed was 10 mm/h. Back-scattered Laue diffraction was used to check the single-crystalline state and to orient the crystal for magnetic-susceptibility, magnetization, specific-heat, and ultrasound measurements.

Single crystal x-ray diffraction data were collected at ambient temperature using a four-circle diffractometer (Gemini of Agilent) equipped with a Mo x-ray tube [$\lambda(\text{MoK}\alpha) = 0.71073 \text{ \AA}$], Mo-enhanced collimator, graphite monochromator, and an Atlas CCD detector. The CrysAlis Pro [31] program was used for lattice indexing, to refine the unit cell, reduce the data, and perform the absorption correction (face-indexing and Gaussian spherical harmonics algorithms). Superflip [32] was employed to solve the structure. Refinements of the crystal structure were carried out using Jana2006 [33] against all the reflections. The final R -factor for the crystal structure solved in the space group $P6_3/mmc$ (type $\text{Gd}_3\text{Ru}_4\text{Al}_{12}$) converged to 3.2%. The lattice parameters of $\text{U}_3\text{Ru}_4\text{Al}_{12}$ were found to be $a = 8.828(3) \text{ \AA}$ and $c = 9.430(4) \text{ \AA}$, which are in good agreement with those reported in Refs. [14, 15].

Magnetic susceptibility (an excitation with an amplitude of $\mu_0 H_{\text{exc}} = 0.001 \text{ T}$ was applied along the [100] and [120] axes at a frequency of 97 Hz) and magnetization in static magnetic fields up to 14 T were measured using a commercial Physical Property Measurement System (PPMS). The PPMS was also used for specific-heat measurements by the relaxation method.

High-field magnetization was measured at 2 K in pulsed magnetic fields up to 58 T by the induction method using a coaxial pick-up coil system (a detailed description of the magnetometer can be found in Ref. [34]). Absolute values of the magnetization were calibrated using data obtained in static fields.

The field and temperature dependences of the relative sound-velocity changes, $\Delta v/v$, were measured using an ultrasound pulse-echo technique [35, 36] in static magnetic fields up to 17 T and in pulsed magnetic fields up to 58 T. A pair of piezoelectric transducers were glued to opposite surfaces of the sample in order to excite and detect acoustic waves. We approximated the relative changes of the elastic moduli, $\Delta C_{ii}/C_{ii}$, using $\Delta C_{ii}/C_{ii} \approx 2\Delta v_{ii}/v_{ii}$ for small sound velocity changes. We measured the longitudinal, C_{11} ($\mathbf{k} \parallel \mathbf{u} \parallel [100]$), where \mathbf{k} and \mathbf{u} are the wavevector and polarization of acoustic waves, respectively), C_{33} ($\mathbf{k} \parallel \mathbf{u} \parallel [001]$), and transverse, C_{44} ($\mathbf{k} \parallel [100], \mathbf{u} \parallel [001]$), C_{66} ($\mathbf{k} \parallel [100], \mathbf{u} \parallel [120]$) acoustic modes. The magnetic field was applied along the [100] and [120] axes.

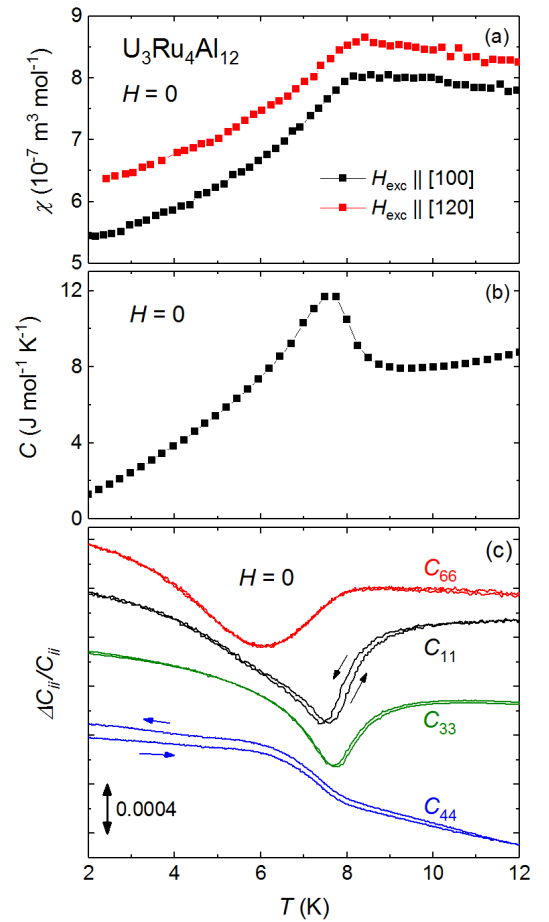


FIG. 1: Temperature dependences of (a) the magnetic susceptibility, χ , (b) the specific heat, C , and (c) the relative change of the elastic moduli C_{11} , C_{33} , C_{44} , and C_{66} of $\text{U}_3\text{Ru}_4\text{Al}_{12}$ at zero field. The ultrasound frequencies were 56, 98, 29, and 124 MHz for the C_{11} , C_{33} , C_{44} , and C_{66} modes, respectively.

III. RESULTS

Figure 1(a) shows the magnetic susceptibility, χ , of $\text{U}_3\text{Ru}_4\text{Al}_{12}$ in zero field. An antiferromagnetic order sets in at around 8 K where χ starts to decrease for both [100] and [120] excitation directions. The χ vs. T data agree well with previous results and can be explained by ordering of the magnetic moments in the basal plane as found by neutron scattering [15]. [001] is a hard axis. χ does not display anomalies for $H_{\text{exc}} \parallel [001]$ (not shown).

The specific heat, C , displays a lambda-type anomaly [Fig. 1(b)]. We define the midpoint of the specific-heat increase as the Néel temperature, $T_N = 8.2 \text{ K}$.

Near T_N , all elastic moduli show anomalies that point to the magnetoelastic coupling in $\text{U}_3\text{Ru}_4\text{Al}_{12}$ [Fig. 1(c)]. C_{11} and C_{33} have minima near T_N . C_{44} displays hardening upon entering the antiferromagnetic state. C_{66} starts softening at T_N and shows a minimum centered at 6 K. As will be shown below, the broad anomalies in C_{44} and C_{66} originate from two successive phase transitions.

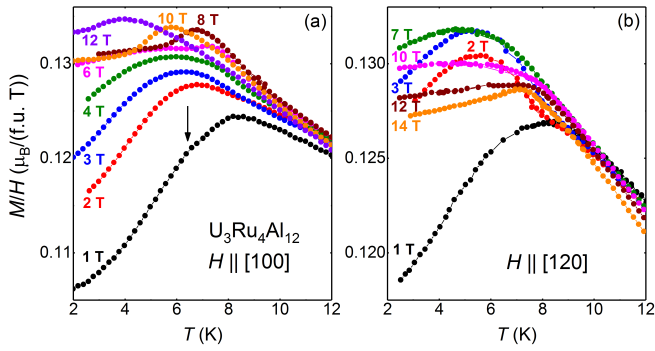


FIG. 2: Temperature dependences of the magnetization, M , divided by field, H , applied along the (a) [100] and (b) [120] axes of $U_3Ru_4Al_{12}$.

In applied field, the magnetic susceptibility does not show any clear anomaly. We used magnetization divided by field, M/H , and elastic moduli to trace the field evolution of various magnetic phases in $U_3Ru_4Al_{12}$.

For a field of 1 T applied along the [100] axis, M/H displays a pronounced decrease on entering the antiferromagnetic state [Fig. 2(a)]. Apart from a maximum at 8 K, a small bump can be resolved near 6 K as indicated by an arrow. This suggests the presence of two transitions. They exhibit a broad maximum in M/H in fields up to 4 T. A sharper anomaly emerges at higher magnetic fields. It is found close to T_N in zero field and, hence, signals an antiferromagnetic-paramagnetic phase transition.

M/H for field applied along the [120] axis also shows a broad maximum [Fig. 2(b)]. It shifts to lower temperatures with field up to 10 T. At higher fields, a kink is observed, e.g., at 7 K in 14 T. It likely indicates a phase transition from the antiferromagnetic into the paramagnetic state.

Thus, our magnetization data allow us to follow the field evolution of the Néel temperature and point to additional anomalies below T_N . Our measurements of elastic moduli provide further evidence for new phases in $U_3Ru_4Al_{12}$.

For field applied along the [100] axis, C_{11} and C_{33} display a minimum at the Néel temperature that broadens with increasing field [Figs. 3(a) and 3(b)]. At 12 T, T_N is reduced to about 4 K.

C_{44} and C_{66} show a change of the slope and a minimum, respectively [Figs. 3(c) and (d)]. These features shift to lower temperatures with increasing field and are no longer observed above 4 T. Therefore, they most likely have an origin different from the antiferromagnetic-paramagnetic phase transition. The transitions seen in C_{44} and C_{66} correspond to the broad maxima in M/H [Fig. 2(a)]. A phase transition into the paramagnetic state can be identified by an inflection point of C_{44} and C_{66} .

All elastic moduli show a single anomaly for field applied along the [120] direction (Fig. 4). C_{11} and C_{33} exhibit a minimum near the Néel temperature that broad-

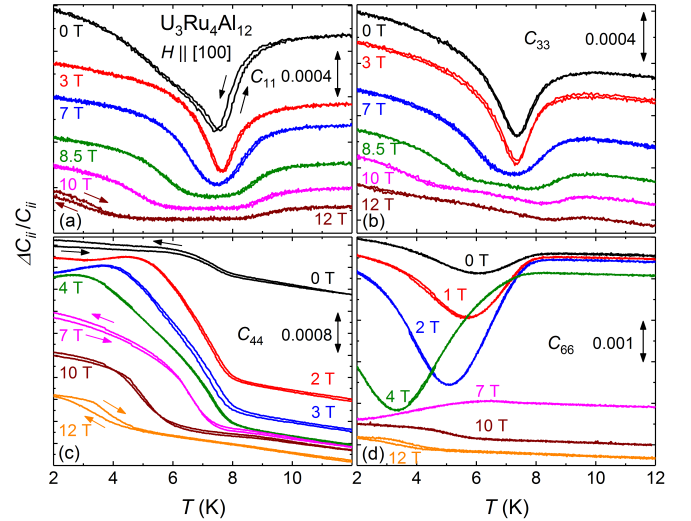


FIG. 3: Temperature dependences of the relative change of the elastic moduli (a) C_{11} , (b) C_{33} , (c) C_{44} , and (d) C_{66} for field applied along the [100] axis of $U_3Ru_4Al_{12}$. The ultrasound frequencies were 56, 89, 29, and 124 MHz for the C_{11} , C_{33} , C_{44} , and C_{66} modes, respectively.

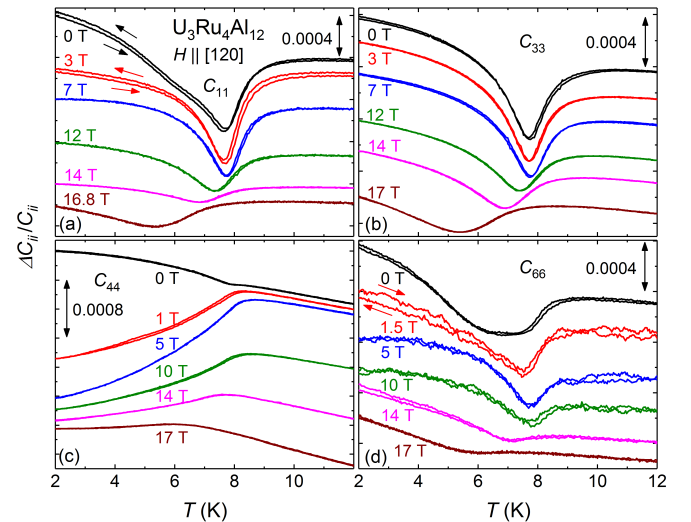


FIG. 4: Temperature dependences of the relative change of the elastic moduli (a) C_{11} , (b) C_{33} , (c) C_{44} , and (d) C_{66} for field applied along the [120] axis of $U_3Ru_4Al_{12}$. The ultrasound frequencies were 64, 98, 30, and 112 MHz for the C_{11} , C_{33} , C_{44} , and C_{66} modes, respectively.

ens and shifts to lower temperatures with increasing field [Figs. 4(a) and 4(b)].

With decreasing temperature, C_{44} shows hardening in zero field with a kink at T_N [Fig. 4(c)]. This changes to softening in 1 T, which suggests a large transformation of the magnetic state, probably due to a transition to a new phase. The broad minimum in C_{66} observed in zero field narrows in applied fields [Fig. 4(d)], probably due to the appearance of a new magnetic phase.

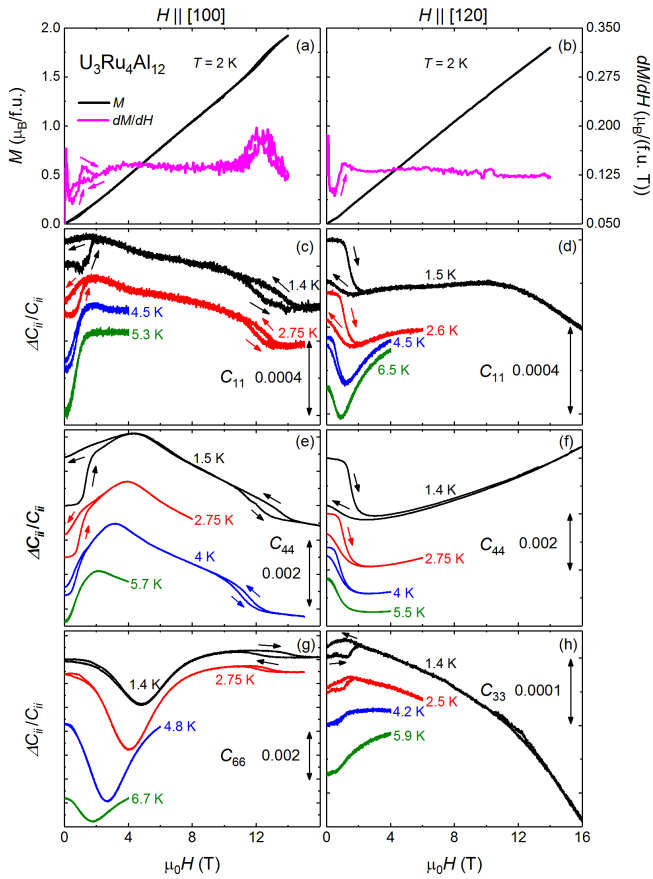


FIG. 5: Field dependences of (a) and (b) the magnetization, M , and the field derivative of the magnetization, dM/dH ; and the relative change of the elastic moduli (c) and (d) C_{11} , (e) and (f) C_{44} , (g) C_{66} , and (h) C_{33} for field applied along the [100] and [120] axis of $U_3Ru_4Al_{12}$. For field applied along the [100] axis, the ultrasound frequencies were 56, 29, and 124 MHz for the C_{11} , C_{44} , and C_{66} modes, respectively. For field applied along the [120] axis, the ultrasound frequencies were 64, 30, and 98 MHz for the C_{11} , C_{44} , and C_{33} modes, respectively.

For field applied along the [100] direction at 2 K, the magnetization displays a weak change of slope near 12 T [Fig. 5(a)]. The field derivative of the magnetization, dM/dH , shows an anomaly with hysteresis at low fields and a maximum just above 12 T. Additional field-induced transitions can be revealed in the elastic moduli. C_{11} and C_{44} show hardening just below 2 T at 1.4 and 1.5 K, respectively [Figs. 5(c) and 5(e)]. The hardening has large hysteresis which does not close when sweeping the field back to zero. For C_{44} , a pronounced maximum is also observed near 4 T at 1.5 K. In the same field range, C_{66} shows a minimum [Fig. 5(g)]. Additionally, C_{11} , C_{44} , and C_{66} display a broad field-induced transition above 12 T as the antiferromagnetic order is suppressed [Figs. 5(c), 5(e), and 5(g)].

For field applied along the [120] axis, the magnetization is a smooth function of field up to 14 T at 2 K [Fig.

5(b)]. dM/dH shows an anomaly at 1 T. This transition leads to softening of C_{11} and C_{44} [Figs. 5(d) and 5(f)] and hardening of C_{33} [Fig. 5(h)]. For C_{44} , this is in accordance with our observation that hardening changes to softening between zero and 1 T at T_N as the temperature decreases [Fig. 4(c)]. We find no other transitions in fields up to 16 T.

For C_{33} ($\mathbf{H} \parallel [100]$) and C_{66} ($\mathbf{H} \parallel [120]$), no anomalies can be resolved (not shown).

Our magnetization and elastic-modulus measurements in static fields up to 17 T suggest that $U_3Ru_4Al_{12}$ shows several distinct phases below T_N . We have found evidence for the existence of three magnetic phases for field applied along the [100] axis. Two phases were revealed for field applied along the [120] axis. Higher magnetic fields are required since $U_3Ru_4Al_{12}$ may display additional field-induced transitions.

Figure 6(a) shows the magnetization measured in pulsed magnetic field up to 58 T applied along the principal crystallographic directions of $U_3Ru_4Al_{12}$ at 1.7 K. A large magnetic anisotropy is evident between the basal plane and the [001] axis. The easy-magnetization direction lies in the basal plane, in accordance with the neutron-scattering data [15]. An anomaly with hysteresis is found in the vicinity of 13 T for field applied along the [100] axis. The field derivative of the magnetization, dM/dH , shows maxima at 15 and 11 T for up and down field sweeps, respectively [inset in Fig. 6(a)]. In the same field range, C_{44} displays a broad anomaly that originates from a suppression of the antiferromagnetic order [Fig. 5(e)]. For field applied along the [120] axis, dM/dH also shows a maximum at 19 T. Above 30 T, the magnetization for $\mathbf{H} \parallel [100]$ and $\mathbf{H} \parallel [120]$ tends to level off and reaches approximately $3.5 \mu_B/\text{f.u.}$ Taking into account the rather large magnetic moment per uranium atom, $M_U = 2.5 \mu_B$ [15], more transitions can be expected in higher fields. The magnetization per f.u. of the forced ferromagnetic state can be found as follows: $M_{\text{ferro}} = 3 \times M_U = 7.5 \mu_B$. For $\mathbf{H} \parallel [001]$, the magnetization shows no anomalies.

Since C_{44} displays pronounced anomalies as a function of temperature and field, we also measured this elastic modulus in pulsed fields. C_{44} displays softening for $\mathbf{H} \parallel [100]$ [Fig. 6(b)]. In addition to the transitions found in static fields [Fig. 5(e)], we observe an inflection point between 20 and 30 T. In the same field interval, the magnetization changes its slope. These anomalies probably mark a crossover to a new phase. For $\mathbf{H} \parallel [120]$, the softening observed in low fields is followed by pronounced hardening [Fig. 6(c)]. A kink is seen around 20 T. Near this field, dM/dH shows a maximum [inset in Fig. 6(a)].

Figure 7 shows the H - T phase diagram of $U_3Ru_4Al_{12}$ based on our magnetization and elastic-modulus measurements. The diagram strongly depends on the field direction, which points to a large anisotropy of the magnetic and elastic properties. For field applied along the [100] axis, three distinct phases exist below T_N [Fig. 7(a)]. Phase I exists in the low temperature-low field cor-

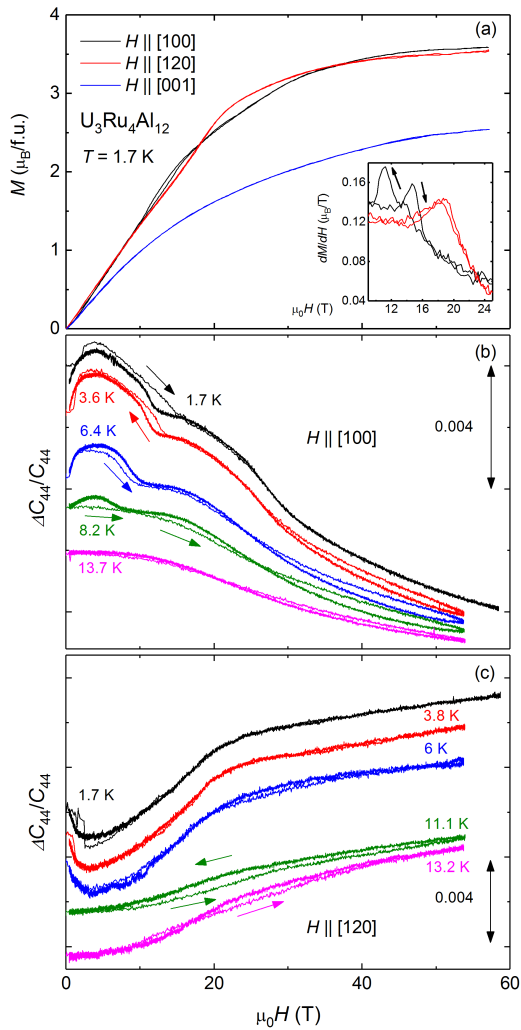


FIG. 6: Field dependences of (a) the magnetization, M , for field applied along the [100], [120], and [001] axes and (b) and (c) the relative change of the elastic modulus C_{44} for field applied along the [100] and [120] axes of $U_3Ru_4Al_{12}$. The inset in panel (a) shows the field derivatives of the magnetization, dM/dH , for field applied along the [100] and [120] axes. The ultrasound frequencies were 111 and 104 MHz for field applied along the [100] and [120] axes, respectively.

ner. With increasing field, phase I changes to an intermediate phase II at 2 T. Near 6 T, $U_3Ru_4Al_{12}$ enters phase III. At the lowest temperatures, the antiferromagnetic-paramagnetic phase boundary is found at about 13 T. The critical field of a high-field anomaly in the paramagnetic state found for C_{44} in pulsed fields is also shown in Fig. 7(a).

Two phases can be found for field applied along the [120] axis [Fig. 7(b)]. Here, the ordered phase is suppressed at 19 T. Phase V exists below the paramagnetic-antiferromagnetic phase boundary in a broad field range. Below 1.5 T, $U_3Ru_4Al_{12}$ shows phase IV. This is likely the same phase as phase I for $H \parallel [100]$ as both of them occur in a small region close to zero field. A possible

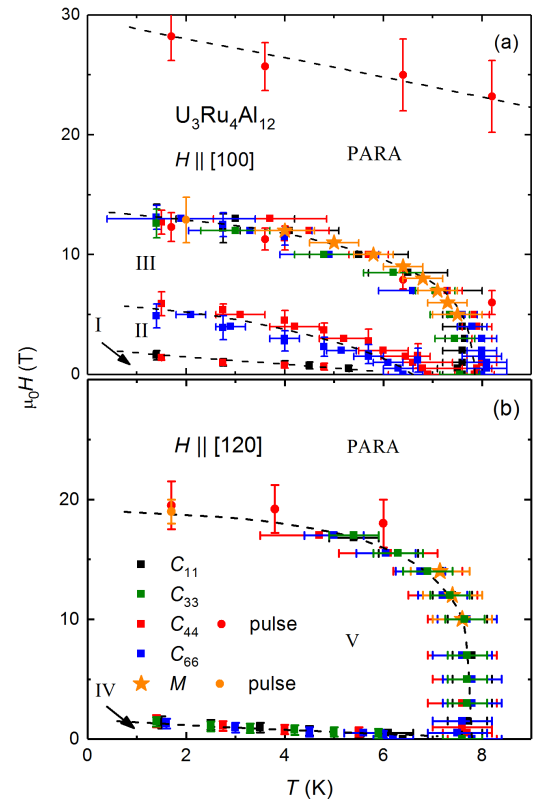


FIG. 7: Magnetic phase diagrams for field applied along (a) the [100] and (b) the [120] axes of $U_3Ru_4Al_{12}$. Lines are guides to the eye.

nature of the observed phases will be discussed in Sec. V.

IV. CEF ANALYSIS

For uranium-based intermetallic compounds, CEF effects are usually not so pronounced as compared to rare-earth-based materials. This is due to the extended $5f$ wavefunctions in contrast to the well localized $4f$ wavefunctions. Nevertheless, for some uranium-based compounds, e.g., $UNiSn$ and UCu_2Sn , pronounced CEF effects and concomitant softening of a transverse elastic modulus were observed [37, 38].

For $U_3Ru_4Al_{12}$, there is a large softening of C_{44} below 100 K, whereas C_{11} , C_{33} , and C_{66} show hardening with decreasing temperature down to T_N (Fig. 8). Below, we explain this softening by CEF effects.

For a CEF analysis, we have to make an assumption about the state of the $5f$ electrons in $U_3Ru_4Al_{12}$. Previous results showed a reduced ordered uranium magnetic moment as compared to the $5f^2$ and $5f^3$ configurations [14, 15]. Additionally, the electrical resistivity is either constant or decreases strongly with temperature in the paramagnetic state, depending on the direction of current. This suggests that the $5f$ electrons are

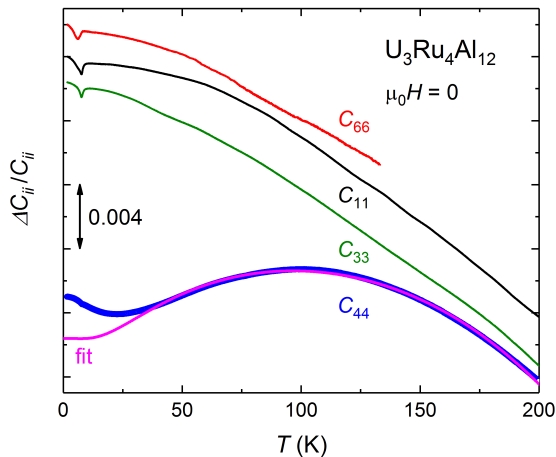


FIG. 8: Relative change of the elastic moduli C_{11} , C_{33} , C_{44} , and C_{66} of $\text{U}_3\text{Ru}_4\text{Al}_{12}$ at zero field. The ultrasound frequencies were 64, 98, 29, and 124 MHz for the C_{11} , C_{33} , C_{44} , and C_{66} modes, respectively. The magenta curve is a fit of C_{44} using Eq. (6).

likely more delocalized at high temperatures, i.e., uranium approaches the $5f^2$ state. Therefore, we assumed the $5f^2$ configuration of uranium for the CEF analysis in the paramagnetic state of $\text{U}_3\text{Ru}_4\text{Al}_{12}$.

We used the CEF model to fit our magnetization and elastic-modulus data [39, 40]. We start with the effective Hamiltonian,

$$H_{\text{eff}} = H_{\text{CEF}} + H_{\text{sQ}} + H_{\text{QQ}} + H_{\text{Zeeman}}, \quad (1)$$

where H_{CEF} , H_{sQ} , H_{QQ} , and H_{Zeeman} are the CEF, strain-quadrupole, quadrupole-quadrupole, and Zeeman energy, respectively. In the hexagonal symmetry of $\text{U}_3\text{Ru}_4\text{Al}_{12}$, the CEF term is given by

$$H_{\text{CEF}} = B_2^0 O_2^0 + B_4^0 O_4^0 + B_6^0 O_6^0 + B_6^6 O_6^6, \quad (2)$$

where B_m^n are crystal-field parameters and O_m^n are Stevens' equivalent operators [41]. The strain-quadrupole interaction can be expressed as

$$H_{\text{sQ}} = - \sum_i g_i O_i \varepsilon_i, \quad (3)$$

where g_i is the strain-quadrupole coupling constant, O_i is the quadrupole operator, and ε_i is the strain. The quadrupole-quadrupole interaction is

$$H_{\text{QQ}} = - \sum_i g'_i \langle O_i \rangle O_i, \quad (4)$$

where g'_i is the quadrupole-quadrupole coupling constant and $\langle O_i \rangle$ is a thermal average of the operator O_i . The Zeeman energy is

$$H_{\text{Zeeman}} = -g_j \mu_B J H, \quad (5)$$

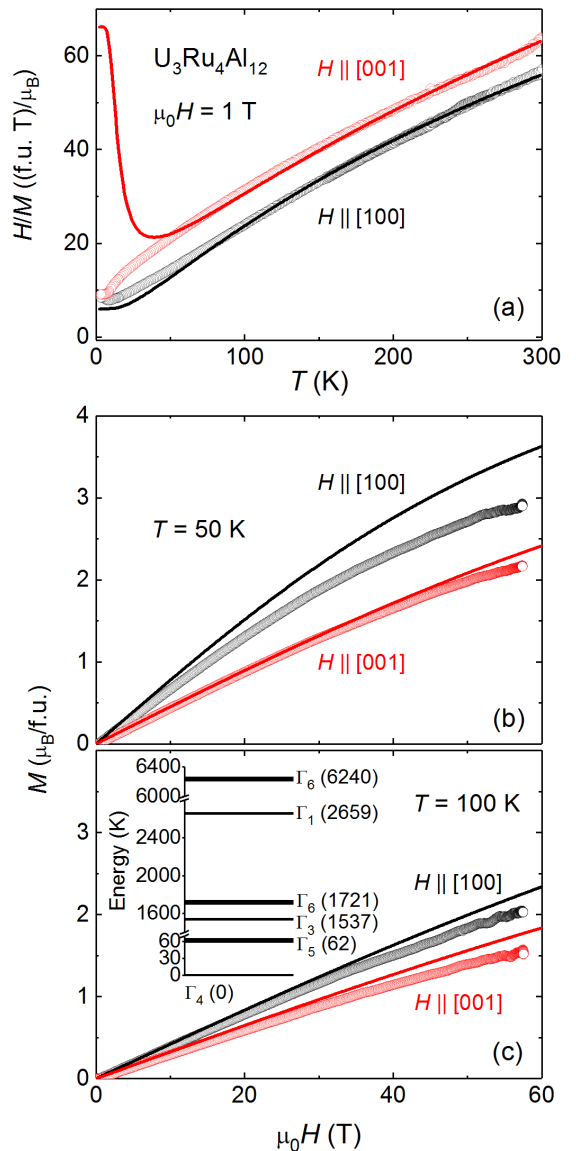


FIG. 9: (a) Temperature dependences of H/M measured in a field of 1 T and field dependences of the magnetization, M , up to 58 T at (b) 50 K and (c) 100 K for $\text{U}_3\text{Ru}_4\text{Al}_{12}$. In all panels, the symbols and the solid lines represent the experimental and calculated data, respectively. The inset in panel (c) shows the CEF level scheme of a U^{4+} ($J = 4$) ion obtained from the CEF parameters listed in Table I. In the inset, the thin lines represent singlets, the thick lines represent doublets.

where $g_j = 0.8$ is the Landé factor and $J = 4$ is the quantum number of the total angular momentum of a U^{4+} ion.

The temperature dependence of an elastic modulus C_{ii} can be calculated using the equation

$$C_{ii}(T) = C_{ii}^{(0)}(T) - \frac{N_0 g_i^2 \chi_i^{(s)}(T)}{1 - g'_i \chi_i^{(s)}(T)}, \quad (6)$$

that takes into account quadrupolar interactions. Here,

TABLE I: CEF parameters, B_m^n (K), for $U_3Ru_4Al_{12}$.

B_2^0	B_4^0	B_6^0	B_6^6
87.9(5)	1.8(3)	-0.009(1)	0.31(3)

$C_{ii}^{(0)}$ is the background stiffness, $N_0 = 9.39 \times 10^{27} \text{ m}^{-3}$ is the density of U atoms per unit volume, $\chi_i^{(s)}$ is a quadrupolar susceptibility [35]. More detailed information about the CEF analysis is given in the Supplemental Material [42].

Using the CEF parameters listed in Table I, we could reproduce the temperature variation of H/M between 80 and 300 K [Fig. 9(a)]. At low temperatures for field applied along the [001] axis, the calculated H/M grows, whereas the experimental H/M continues to decrease. This discrepancy can likely be explained by changes in the localization degree of the $5f$ electrons and the appearance of other contributions on approaching the ordered state such as Kondo-like interactions [15].

The magnetization in fields up to 58 T is qualitatively reproduced at 50 and 100 K [Figs. 9(b) and (c)]. The agreement between theory and experiment is better at 100 K.

Our model also reproduces the softening of C_{44} (Fig. 8) in the same temperature range as H/M [Fig. 9(a)]. Using Eq. (6), we obtained $g_i = 162.6$ K and $g'_i = -5.18$ K. The negative g'_i value suggests the existence of antiferroquadrupolar-type interactions.

In a hexagonal CEF, the 9-fold multiplet of U^{4+} splits into 3 singlets and 3 doublets [inset in Fig. 9(c)]. The ground-state singlet Γ_4 is separated from the first excited doublet Γ_5 by 62 K. The next CEF levels have much higher energies, above 1500 K. The overall CEF splitting exceeds 6000 K.

In the crystal lattice of $U_3Ru_4Al_{12}$, the matrix elements $\langle \Gamma_4 | O_{yz} | \Gamma_4 \rangle$ and $\langle \Gamma_4 | O_{zx} | \Gamma_4 \rangle$ are zero, where O_{yz} and O_{zx} are quadrupole operators. Therefore, for the ground state there is no quadrupolar degeneracy corresponding to the C_{44} mode. The energy separation between the ground state and the first excited state, 62 K, makes the existence of an interlevel quadrupolar interaction possible. The matrix elements $\langle \Gamma_4 | O_{yz} | \Gamma_5 \rangle$ and $\langle \Gamma_4 | O_{zx} | \Gamma_5 \rangle$ have nonzero values. This interlevel quadrupolar interaction explains the softening of C_{44} .

V. DISCUSSION

The electronic properties of uranium-based intermetallic compounds are largely determined by the unfilled $5f$ shell. The $5f$ wavefunctions are more extended as compared to the $4f$ wavefunctions of the rare-earth elements, resulting in a greater hybridization with valence and conduction electrons. The $5f$ states of a vast majority of uranium intermetallics are itinerant, or partly itinerant [10, 43, 44]. On the one hand, the extended hybridization delocalizes the $5f$ electrons and leads to a loss of mag-

netic order. On the other hand, it promotes magnetic coupling between the $5f$ sites. An empirical rule for the formation of a magnetic order is given by a critical value of the distance between nearest-neighbor uranium ions, known as the Hill limit [45]. If the inter-uranium spacing exceeds 3.4 - 3.6 Å, a spontaneous magnetic order of the uranium sublattice may exist. However, Hill's rule is not always valid and should rather be taken as an indication whether the $5f$ electrons can be localized (see, e.g., Refs. [46, 48, 49, 57]).

Another important consequence of the extended hybridization of the $5f$ states is the magnetic anisotropy. It is related to the bonding anisotropy in the sense that the direction of magnetic moments is determined by the bonding symmetry. As a result, the U magnetic moments tend to align as far as possible from the nearest-neighbor U-U links [50]. In uniaxial crystal structures, e.g., hexagonal and tetragonal, the moments are oriented perpendicular to the shortest inter-uranium spacings. The strong spin-orbit coupling leads to a very large magnetic anisotropy and a prevalence of collinear magnetic structures, whereby the magnetic moments are locked along high-symmetry directions.

$U_3Ru_4Al_{12}$ displays unusual magnetic properties that do not completely follow this conventional picture. The U atoms form a kagome lattice parallel to the basal plane where the shortest inter-uranium distances, 3.575 Å, are found. This value is within the Hill limit, and one could expect a small localized moment, if any. However, $U_3Ru_4Al_{12}$ shows a rather large magnetic moment, $2.5 \mu_B/U$ atom, as found by neutron scattering [15]. For a CEF analysis, we assumed the $5f^2$ state of uranium in the paramagnetic region and found a better agreement between experiment and theory at 100 K than at 50 K. Further, the direction of the U magnetic moments is not perpendicular to the shortest inter-uranium spacings. This would require the moments to be oriented parallel to the hexagonal 6-fold axis. Unexpectedly, the U magnetic moments are arranged in a noncollinear triangular structure in the basal plane [15].

The unanticipated ground-state magnetic properties of $U_3Ru_4Al_{12}$ can be tuned by an external parameter to study the exchange interactions and magnetic anisotropy and reveal the role of a possible geometric frustration. We have found that the magnetic and elastic properties of $U_3Ru_4Al_{12}$ are particularly susceptible to applied magnetic fields.

The H - T phase diagram of $U_3Ru_4Al_{12}$ features three phases for $\mathbf{H} \parallel [100]$ and two phases for $\mathbf{H} \parallel [120]$ below the Néel temperature. The transitions between these phases lead to pronounced anomalies in elastic moduli due to the existence of magnetoelastic coupling. This makes ultrasound measurements extremely useful for mapping out the phase diagram.

Since the U atoms are coupled antiferromagnetically and form a kagome lattice, competing exchange interactions are a likely reason for the existence of several phases in the H - T diagram of $U_3Ru_4Al_{12}$. Apart from the

peak due to the paramagnetic-antiferromagnetic transition, our zero-field specific-heat data do not show other anomalies [Fig. 1(b)]. This suggests that the magnetic entropy changes little when passing from one phase into the other.

Below, we discuss the nature of zero-field and field-induced phases in terms of their possible magnetic-moment configurations. The magnetic structure of $U_3Ru_4Al_{12}$ was determined to be commensurate non-collinear with the moments confined to the basal plane at 1.6 K [15]. The representation analysis indicates that only one two-dimensional (2D) physically irreducible representation (irrep) is active in the model described in Ref. [15] (mGM5- in the Miller and Love notation [51]). In fact, further symmetry analysis of the solution using the tools of Bilbao Crystallographic Server [52, 53] shows that the spin configuration corresponds to the Shubnikov space group $Cmcm'$, for which two different irreps are found to be active instead of one. In addition to the primary 2D irrep, mGM5-, a secondary unidimensional irrep, mGM2-, allows additional degrees of freedom for the spins in this structure. In the model described in Ref. [15], the magnetic ordering splits the magnetic site into two independent sites with distinct degrees of freedom for the U spins. Nevertheless, spin amplitude and orientation seem to be correlated with those of the primary active irrep. Hence, some relative spin orientations not forced by symmetry were probably included in the model [53], although certainly fully supported by the experimental data.

It follows from our magnetic-susceptibility and magnetization data that the U magnetic moments do not deviate from the basal plane below T_N . As the temperature is raised above 6 K, a different magnetic state emerges. Given that the geometrical arrangement of the U atoms likely frustrates exchange interactions, it is reasonable to expect a magnetic structure that is incommensurate with the unit cell.

Although rare, incommensurate magnetic structures have been found for some uranium intermetallics. An incommensurate helical structure was reported for UPtGe where it forms due to the coexistence of a small in-plane magnetic anisotropy and frustrated exchange interactions [54, 55]. Another example is UNiGe that shows an incommensurate phase between 41.5 K and $T_N = 51$ K [56–58]. Below 41.5 K, a commensurate antiferromagnetic phase exists [57–59]. For $U_3Ru_4Al_{12}$, no temperature dependence of the magnetic wavevector is given in Ref. [15]. As the magnetic structure likely changes in the vicinity of 6 K, an additional zero-field neutron-scattering study is required to follow its temperature evolution.

The antiferromagnetic order of $U_3Ru_4Al_{12}$ does not seem particularly robust as relatively small fields, ≈ 1 T, break it. This reflects that the ground state can be

easily perturbed due to geometric frustration. The field-induced states have a nonzero ferromagnetic component. Since the magnetization is far from the forced ferromagnetic state even in fields up to 58 T, the ferromagnetic component coexists with an antiferromagnetic component. This was observed for the field-induced phases of UNiGe [56, 60–62].

A small magnetic moment might be induced on the Ru atoms in applied field as well. $U_3Ru_4Al_{12}$ has a large C/T value, ≈ 600 mJ mol $^{-1}$ K $^{-2}$ [15], close to that of $Dy_3Ru_4Al_{12}$, ≈ 500 mJ mol $^{-1}$ K $^{-2}$ [16]. As explained for $Dy_3Ru_4Al_{12}$, the Ru $4d$ subsystem is involved in the exchange interactions due to the polarization coming from the $4f$ and $5d$ states. A similar effect likely exists for $U_3Ru_4Al_{12}$, whereby the Ru $4d$ states are polarized through the $5f$ and $6d$ states. In applied field, the splitting of the spin-up and spin-down subbands of the itinerant $4d$ states grows, and the Ru magnetic moment increases.

We can speculate about an additional broad high-field feature in C_{44} in the paramagnetic state for field applied along the [100] axis [Fig. 6(b)]. It probably originates from changes of the U magnetic moment. As the magnetization continues to increase in this field range, the U moments may become more localized. If this picture is correct, the band structure should be affected. Therefore, electrical-resistivity measurements in high fields may provide more information about the physics of the $5f$ states of $U_3Ru_4Al_{12}$.

VI. CONCLUSION

Our results reveal an important role of geometric frustration and CEF effects in the physical properties of $U_3Ru_4Al_{12}$. We observed several distinct ordered phases when field is applied along the basal plane. Our CEF analysis suggests that the quadrupolar interactions result in a pronounced elastic softening of the shear modulus C_{44} . Thus, $U_3Ru_4Al_{12}$ is a good candidate for magnetic x-ray and neutron scattering studies of frustration effects.

VII. ACKNOWLEDGEMENTS

The work was supported by the project 16-03593S of the Czech Science Foundation and by the Materials Growth and Measurement Laboratory (MGML, <https://mgml.eu>). We acknowledge the support of HLD at HZDR, member of the European Magnetic Field Laboratory (EMFL), and the DFG through SFB 1143.

[1] I. S. Hagemann, Q. Huang, X. P. A. Gao, A. P. Ramirez, and R. J. Cava, Phys. Rev. Lett. **86**, 894 (2001).

[2] X. G. Zheng, H. Kubozono, K. Nishiyama, W. Higemoto,

- T. Kawae, A. Koda, and C. N. Xu, *Phys. Rev. Lett.* **95**, 057201 (2005)
- [3] J. S. Gardner, M. J. P. Gingras, and J. E. Greedan, *Rev. Mod. Phys.* **82**, 53 (2010).
- [4] P. Khuntia, F. Bert, P. Mendels, B. Koteswararao, A. V. Mahajan, M. Baenitz, F. C. Chou, C. Baines, A. Amato, and Y. Furukawa, *Phys. Rev. Lett.* **116**, 107203 (2016).
- [5] Y. Zhou, K. Kanoda, and T. K. Ng, *Rev. Mod. Phys.* **89**, 025003 (2017).
- [6] Q. Luo, S. Hu, B. Xi, J. Zhao, and X. Wang, *Phys. Rev. B* **95**, 165110 (2017).
- [7] A. Dönni, G. Ehlers, H. Maletta, P. Fischer, H. Kitazawa, and M. Zolliker, *J. Phys. Condens. Matter* **8**, 11213 (1996).
- [8] V. Fritsch, N. Bagrets, G. Goll, W. Kittler, M. J. Wolf, K. Grube, C. L. Huang, and H. v. Löhneysen, *Phys. Rev. B* **89**, 054416 (2014).
- [9] S. Lucas, K. Grube, C. L. Huang, A. Sakai, S. Wunderlich, E. L. Green, J. Wosnitzer, V. Fritsch, P. Gegenwart, O. Stockert, and H. v. Löhneysen, *Phys. Rev. Lett.* **118**, 107204 (2017).
- [10] V. Sechovský and L. Havela, in *Handbook of Magnetic Materials*, edited by K. H. J. Buschow (Elsevier, Amsterdam, 1998), Vol. 11.
- [11] R. E. Gladyshevskii, O. R. Strusievicz, K. Cenual, and E. Parthé, *Acta Cryst. B* **49**, 474 (1993).
- [12] J. Niermann and W. Jeitschko, *Z. Anorg. Allg. Chem.* **628**, 2549 (2002).
- [13] N. G. Bukhan'ko, A. I. Tursina, S. V. Malyshev, A. V. Gribov, Y. D. Seropegin, and O. I. Bodak, *J. Alloys Compd.* **367**, 149 (2004).
- [14] M. Pasturel, O. Tougait, M. Potel, T. Roisnel, K. Wochowski, H. Noël, and R. Troć, *J. Phys.: Condens. Matter* **21**, 125401 (2009).
- [15] R. Troć, M. Pasturel, O. Tougait, A. P. Sazonov, A. Gukasov, C. Sułkowski, and H. Noël, *Phys. Rev. B* **85**, 064412 (2012).
- [16] D. I. Gorbunov, M. S. Henriques, A. V. Andreev, A. Gukasov, V. Petříček, N. V. Baranov, Y. Skourski, V. Eigner, M. Paukov, J. Prokleška, and A. P. Gonçalves, *Phys. Rev. B* **90**, 094405 (2014).
- [17] S. Nakamura, S. Toyoshima, N. Kabeya, K. Katoh, T. Nojima, and A. Ochiai, *Phys. Rev. B* **91**, 214426 (2015).
- [18] D. I. Gorbunov, M. S. Henriques, A. V. Andreev, Y. Skourski, and M. Dušek, *J. Alloys Compd.* **634**, 115 (2015).
- [19] D. I. Gorbunov, M. S. Henriques, A. V. Andreev, V. Eigner, A. Gukasov, X. Fabrèges, Y. Skourski, V. Petříček, and J. Wosnitzer, *Phys. Rev. B* **93**, 024407 (2016).
- [20] V. Chandragiri, K. K. Iyer, and E. V. Sampathkumaran, *Intermetallics* **76**, 26 (2016).
- [21] V. Chandragiri, K. K. Iyer, and E. V. Sampathkumaran, *J. Phys.: Cond. Matter* **28**, 286002 (2016).
- [22] D. I. Gorbunov, T. Nomura, I. Ishii, M. S. Henriques, A. V. Andreev, M. Doerr, T. Stöter, T. Suzuki, S. Zherlitsyn, and J. Wosnitzer, *Phys. Rev. B* **97**, 184412 (2018).
- [23] I. Ishii, T. Mizuno, K. Takezawa, S. Kumano, Y. Kawamoto, T. Suzuki, D. I. Gorbunov, M. S. Henriques, and A. V. Andreev, *Phys. Rev. B* **97**, 235130 (2018).
- [24] G. Quirion, M. L. Plumer, O. A. Petrenko, G. Balakrishnan, and C. Proust, *Phys. Rev. B* **80**, 064420 (2009).
- [25] T. Watanabe, S. Hara, S. I. Ikeda, and K. Tomiyasu, *Phys. Rev. B* **84**, 020409(R) (2011).
- [26] V. Tsurkan, S. Zherlitsyn, V. Felea, S. Yasin, Y. Skourski, J. Deisenhofer, H. A. Krug von Nidda, P. Lemmens, J. Wosnitzer, and A. Loidl, *Phys. Rev. Lett.* **106**, 247202 (2011).
- [27] V. Tsurkan, S. Zherlitsyn, S. Yasin, V. Felea, Y. Skourski, J. Deisenhofer, H. A. Krug von Nidda, J. Wosnitzer, and A. Loidl, *Phys. Rev. Lett.* **110**, 115502 (2013).
- [28] S. Zherlitsyn, V. Tsurkan, A. A. Zvyagin, S. Yasin, S. Erfanifam, R. Beyer, M. Naumann, E. Green, J. Wosnitzer, and A. Loidl, *Phys. Rev. B* **91**, 060406(R) (2015).
- [29] G. Quirion, M. Lapointe-Major, M. Poirier, J. A. Quilliam, Z. L. Dun, and H. D. Zhou, *Phys. Rev. B* **92**, 014414 (2015).
- [30] C. Bidaud, O. Simard, G. Quirion, B. Prévost, S. Daneau, A. D. Bianchi, H. A. Dabkowska, and J. A. Quilliam, *Phys. Rev. B* **93**, 060404(R) (2016).
- [31] CrysAlis PRO, Agilent Technologies, Version 1.171.39.46.
- [32] L. Palatinus and G. Chapuis, *J. Appl. Cryst.* **40**, 786 (2007).
- [33] V. Petříček, M. Dušek, and L. Palatinus, *Z. Kristallogr.* **229**, 345 (2014).
- [34] Y. Skourski, M. D. Kuz'min, K. P. Skokov, A. V. Andreev, and J. Wosnitzer, *Phys. Rev. B* **83**, 214420 (2011).
- [35] B. Lüthi, *Physical Acoustics in the Solid State* (Springer, Heidelberg, 2005).
- [36] S. Zherlitsyn, S. Yasin, J. Wosnitzer, A. A. Zvyagin, A. V. Andreev, and V. Tsurkan, *Low Temp. Phys.* **40**, 123 (2014).
- [37] T. Akazawa, T. Suzuki, H. Goshima, T. Tahara, T. Fujita, T. Takabatake, and H. Fujii, *J. Phys. Soc. Jpn.* **67**, 3256 (1998).
- [38] T. Suzuki, I. Ishii, N. Okuda, K. Katoh, T. Takabatake, and T. Fujita, *Phys. Rev. B* **62**, 49 (2000).
- [39] B. Lüthi, *Dynamical Properties of Solids*, edited by G. K. Horton and A. A. Maradudin (North-Holland, Amsterdam, 1980), Vol. 3.
- [40] N. V. Hieu, T. Takeuchi, H. Shishido, C. Tonohiro, T. Yamada, H. Nakashima, K. Sugiyama, R. Settai, T. D. Matsuda, Y. Haga, M. Hagiwara, K. Kindo, S. Araki, Y. Nozue, and Y. Onuki, *J. Phys. Soc. Jpn.* **76**, 064702 (2007).
- [41] M. T. Hutchings, *Solid State Physics* **16**, 227 (1964).
- [42] See Supplemental Material at <http://link.aps.org> for information about the crystal-electric-field analysis.
- [43] J. J. M. Franse, *Helv. Phys. Acta* **56**, 131 (1983).
- [44] J. Lee, M. Matsuda, J. A. Mydosh, I. Zaliznyak, A. I. Kolesnikov, S. Süllow, J. P. C. Ruff, and G. E. Granroth, *Phys. Rev. Lett.* **121**, 057201 (2018).
- [45] H. Hill, *Plutonium*, edited by W. N. Miner (AIME, New York, 1970) 2.
- [46] L. Havela, J. Hřebík, J. Šternberk, A. Meňovský, and A. Zentko, *Phys. Status Solidi (a)* **59**, K165 (1980).
- [47] H. Nakotte, A. Purwanto, R. A. Robinson, Z. Tun, K. Prokeš, A. C. Larson, L. Havela, V. Sechovský, H. Maletta, E. Brück, and F. R. de Boer, *Phys. Rev. B* **54**, 7201 (1996).
- [48] M. S. Henriques, D. I. Gorbunov, J. C. Waerenborgh, L. Havela, A. B. Shick, M. Diviš, A. V. Andreev, and A. P. Gonçalves, *J. Phys.: Condens. Matter* **25**, 066010 (2013).
- [49] M. S. Henriques, D. I. Gorbunov, A. V. Andreev, Z. Arnold, S. Surblé, S. Heathman, J. C. Griveau, E. B. Lopes, J. Prchal, L. Havela, and A. P. Gonçalves, *Phys. Rev. B* **89**, 054407 (2014).

- [50] B. R. Cooper, R. Siemann, D. Yang, P. Thayamballi, and A. Banerjea, in *Handbook on the Physics and Chemistry of the Actinides*, edited by A. J. Freeman and G. H. Lander (Elsevier, Amsterdam, 1985), Vol. 2.
- [51] S. C. Miller and W. F. Love, *Tables of Irreducible Representations of Space Groups and Co-Representations of Magnetic Space Groups* (Pruett, Boulder, 1967); see also A. P. Cracknell, B. L. Davies, S. C. Miller, and W. F. Love, *Kronecker Product Tables*, Vol. 1, (Plenum, New York, 1979).
- [52] J. M. Perez-Mato, S. V. Gallego, E. S. Tasci, L. Elcoro, G. de la Flor, and M. I. Aroyo, *Annu. Rev. Mater. Res.* **45**, 217 (2015).
- [53] S. V. Galego, J. M. Perez-Mato, L. Elcoro, E. S. Tasci, R. M. Hansen, K. Momma, M. I. Aroyo, and G. Madariaga, *J. Appl. Cryst.* **49**, 1750 (2016).
- [54] R. A. Robinson, A. C. Lawson, J. W. Lynn, and K. H. J. Buschow, *Phys. Rev. B* **47**, 6138 (1993).
- [55] L. M. Sandratskii and G. H. Lander, *Phys. Rev. B* **63**, 134436 (2001).
- [56] V. Sechovský, L. Havela, A. Purwanto, A. C. Larson, R. A. Robinson, K. Prokeš, H. Nakotte, E. Brück, F. R. de Boer, P. Svoboda, H. Maletta, and M. Winkelmann, *J. Alloys Compd.* **213-214**, 536 (1994).
- [57] H. Nakotte, A. Purwanto, R. A. Robinson, Z. Tun, K. Prokeš, A. C. Larson, L. Havela, V. Sechovský, H. Maletta, E. Brück, and F. R. de Boer, *Phys. Rev. B* **54**, 7201 (1996).
- [58] G. M. Kalvius, D. R. Noakes, S. El-Khatib, E. J. Ansaldo, C. E. Stronach, E. Brück, and H. Nakotte, *J. Alloys Compd.* **441**, 11 (2007).
- [59] A. Purwanto, V. Sechovský, L. Havela, R. A. Robinson, H. Nakotte, A. C. Larson, K. Prokeš, E. Brück, and F. R. de Boer, *Phys. Rev. B* **53**, 758 (1996).
- [60] H. Nakotte, I. H. Hagmusa, J. C. P. Klaasse, M. S. Torikachvili, A. H. Lacerda, E. Brück, K. Prokes, and F. R. de Boer, *Physica B: Cond. Matter* **246-247**, 441 (1998).
- [61] H. Nakotte, S. Changa, Z. Tun, K. Prokeš, P. Svoboda, V. Sechovský, and E. Brück, *J. Alloys Compd.* **226-230**, 70 (2001).
- [62] K. Prokeš, P. F. de Châtel, E. Brück, F. R. de Boer, K. Ayuel, H. Nakotte, and V. Sechovský, *Phys. Rev. B* **65**, 144429 (2002).